Volume 218 (20) October 2015

Journal of Experimental Biology

The Company of Biologists

© 2015. Published by The Company of Biologists Ltd | Journal of Experimental Biology (2015) 218, 3179-3191 doi:10.1242/jeb.121426

RESEARCH ARTICLE

Feather roughness reduces flow separation during low Reynolds number glides of swifts

Evelien van Bokhorst[1,2], Roeland de Kat[3], Gerrit E. Elsinga[1] and David Lentink[2,*]

ABSTRACT

Swifts are aerodynamically sophisticated birds with a small arm and large hand wing that provides them with exquisite control over their glide performance. However, their hand wings have a seemingly unsophisticated surface roughness that is poised to disturb flow. This roughness of about 2% chord length is formed by the valleys and ridges of overlapping primary feathers with thick protruding rachides, which make the wing stiffer. An earlier flow study of laminar–turbulent boundary layer transition over prepared swift wings suggested that swifts can attain laminar flow at a low angle of attack. In contrast, aerodynamic design theory suggests that airfoils must be extremely smooth to attain such laminar flow. In hummingbirds, which have similarly rough wings, flow measurements on a 3D printed model suggest that the flow separates at the leading edge and becomes turbulent well above the rachis bumps in a detached shear layer. The aerodynamic function of wing roughness in small birds is, therefore, not fully understood. Here, we performed particle image velocimetry and force measurements to compare smooth versus rough 3D-printed models of the swift hand wing. The high-resolution boundary layer measurements show that the flow over rough wings is indeed laminar at a low angle of attack and a low Reynolds number, but becomes turbulent at higher values. In contrast, the boundary layer over the smooth wing forms open laminar separation bubbles that extend beyond the trailing edge. The boundary layer dynamics of the smooth surface varies non-linearly as a function of angle of attack and Reynolds number, whereas the rough surface boasts more consistent turbulent boundary layer dynamics. Comparison of the corresponding drag values, lift values and glide ratios suggests, however, that glide performance is equivalent. The increased structural performance, boundary layer robustness and equivalent aerodynamic performance of rough wings might have provided small (proto) birds with an evolutionary window to high glide performance.

KEY WORDS: Aerodynamic design, Boundary layer, Glide performance, Laminar, Transition

INTRODUCTION

The surface texture of many animals that swim or fly in fluid is tuned to change the dynamics of the boundary layer flow at the surface to reduce drag (Bechert et al., 2000). The precise drag reduction mechanism used depends on the Reynolds number (*Re*, the ratio of inertial and viscous forces). Sharks, for example, operate at a high Reynolds number of the order of millions, for which the boundary layer will transition from laminar to turbulent flow naturally as a result of flow instability. Turbulent flow increases the velocity gradient near the surface, and thus friction drag (Bechert et al., 2000). Sharks reduce this friction drag by reorganizing the structure of the turbulent boundary layer with arrays of riblets that cover their surface (Bechert et al., 1997, 2000; Dean and Bhushan, 2010).

Another way to reduce friction drag is by shaping the body to preserve laminar flow, because laminar boundary layers have much lower friction (Schlichting, 1979; Holmes et al., 1984; White, 1991; Bechert et al., 2000). Unfortunately, laminar boundary layers are also sensitive to small disturbances that can amplify to the point that the flow transitions to turbulence (Hefner and Sabo, 1987). The Reynolds number based on the length it takes a boundary layer to travel and transition naturally is of the order of a million, under minimal disturbance conditions (Schlichting, 1979; White, 1991). Laminar flow-based drag-reduction strategies are therefore within reach for animals swimming and flying at Reynolds numbers below a million. Whereas a low *Re* is a requisite for low drag based on laminar flow, it is not sufficient, because laminar boundary layers are more sensitive to boundary flow separation than turbulent ones (Lissaman, 1983; Simons, 1994; Lyon et al., 1997; Giguère and Selig, 1999; Gopalarathnam et al., 2003; Spedding et al., 2008). Flow separation mostly occurs on the upper side of a wing at a positive angle of attack, due to the strong adverse pressure gradient in the boundary layer (Schlichting, 1979; White, 1991; Mueller, 2002; Shyy, 2013; Kundu and Cohen, 2007). As a result, the flow close to the wall decelerates and comes to a gradual standstill. The boundary layer separates from the surface when the velocity gradient is zero ($du/dy=0$) and reverses direction, which can ultimately result in large-scale flow separation that extends well beyond the trailing edge, i.e. stall. Whereas flow reversal also reverses the orientation of shear stress, and thus reduces friction drag, flow separation increases pressure drag more, and thus increases net drag (Mueller, 2002; Shyy, 2013; Drela, 2014). This drag increase is moderate under certain conditions when the boundary layer re-energizes, reattaches and forms an enclosed separation zone – a so-called 'laminar separation bubble' (Schmidt and Mueller, 1989; Mueller, 2002; Spedding et al., 2008; Shyy, 2013; Drela, 2014).

Re-energization of the boundary layer is facilitated by the boundary layer transition from laminar to turbulent flow, which mixes low energy flow near the wall with higher energy flow in the upper boundary layer (Schlichting, 1979; White, 1991; Mueller, 2002; Shyy, 2013; Drela, 2014). Transition can occur naturally as a result of the boundary layer's sensitivity to small disturbances; alternatively, transition can be promoted by surface roughness and other forms of turbulence generators (Schlichting, 1979; White, 1991; Shyy, 2013). Turbulent boundary layers are less sensitive to flow separation up to a point, and under strong adverse pressure gradients, bigger measures are needed to re-energize the boundary layer, such as vortex generators that reach beyond the boundary layer height (Bechert et al., 2000). They mix high-energy flow outside of the boundary layer with the flow inside as shown by

[1]Department of Mechanical, Maritime and Materials Engineering, Delft University of Technology, Delft 2628 CD, The Netherlands. [2]Department of Mechanical Engineering, Stanford University, Stanford, CA 94305, USA. [3]Engineering and the Environment, University of Southampton, Southampton SO17 1BJ, UK.

*Author for correspondence (dlentink@stanford.edu)

Received 5 March 2015; Accepted 6 August 2015

Journal of Experimental Biology (2015) 218, 3179-3191 doi:10.1242/jeb.121426

List of symbols and abbreviations

c	chord length
C_D	drag coefficient
C_L	lift coefficient
d	primary feather rachis diameter
D	drag
H	shape factor
L	lift
LC	load cell
PIV	particle image velocimetry
Re	Reynolds number
Re_θ	Reynolds number based on momentum thickness
s	span
u	chordwise velocity
u'	chordwise velocity fluctuations
U	tangential velocity at the edge of the boundary layer
U_∞	free-stream velocity
$\overline{u'v'}$	Reynolds shear stress
v'	wall normal velocity fluctuations
v	wall normal velocity
α	angle of attack
δ^*	displacement thickness
δ_{99}	boundary layer thickness
θ	momentum thickness
ρ	density
ω'_z	vorticity fluctuation
μ	dynamic viscosity

Taylor (1947). At the high Reynolds numbers of the pectoral fins of humpback whales, fin serrations at the leading edge generate chordwise vortices that are much larger than the thickness of the boundary layer and mix them effectively, which reduces flow separation and delays stall (Fish and Battle, 1995; Miklosovic et al., 2004; Pedro and Kobayashi, 2008; van Nierop et al., 2008). The reduction of flow separation induced by leading edge serration has also been found on the hand wing of gliding barn owls, which operate at much lower Reynolds numbers (Winzen et al., 2014). The serrations reduce the length of the separation bubble, but remarkably, force measurements did not show a corresponding drag reduction (Winzen et al., 2014), likely an effect due to low Reynolds number.

The Reynolds number at which a boundary layer transitions to a turbulent state depends on the geometry of the surface and its angle of attack with respect to the flow, a process that is still not fully understood in animal flight (Shyy, 2013). Because many insects, bats and birds fly at *Re* below 100,000, the prevailing thought in the literature is that the boundary layer is largely laminar over their wings (Azuma, 2006; Shyy, 2013). Because birds operate at higher Reynolds numbers, and because they are relatively streamlined and efficient (Pennycuick, 2008; Muijres et al., 2012), their wings might critically depend on a particularly well-tuned surface texture. Elimelech and Ellington (2013) found that the wing surface of hummingbirds is rough as a result of the protruding rachides of the hand wing feathers. The effect of this roughness on the boundary layer was studied by measuring the flow field over a 3D printed model of the hummingbird wing. The tests were performed in a wind tunnel that replicates glide conditions at Re=5000 and 15,000, for two geometric angles of attack, α=0 and 10 deg. At low *Re* and low α, they found the flow is mostly laminar, whereas at high *Re* and high α, the boundary layer separates at the leading edge, and subsequently transitions to turbulence above the surface, which enables it to reattach. They concluded: 'The flow mechanism which triggers turbulence is a shear layer which evolves above the wing surface and not the rough texture of the wing surface'. However, neither a control experiment with a smooth model hummingbird wing nor experiments at intermediate α were performed in this study. Such experiments would be insightful, because similar roughness created by strip turbulators is known to trigger transition at the surface and reduce flow separation of model airplanes and drones operating at higher *Re* up to 100,000 and beyond (Braslow and Knox, 1958; Gibbings, 1959; Lissaman, 1983; Simons, 1994; Giguère and Selig, 1999; Gopalarathnam et al., 2003). Model wing studies have, therefore, not fully resolved the influence of feather roughness on boundary layer flow separation, transition and reattachment in bird flight.

The first report of laminar–turbulent flow transition over a real bird wing suggests that the flow over prepared common swift wings is remarkably laminar, despite feather roughness heights of up to 2% chord length. The roughness elements, created by a combination of feather rachides and the overlapping feather vanes, effectively result in corrugated surface analogs to the earlier mentioned strip turbulators (Lentink and de Kat, 2014). A remarkable difference is, however, that theoretical estimates suggest that the roughness height of swift hand wings is similar to the boundary layer thickness (Lentink and de Kat, 2014), whereas in model wings it is a small fraction (Braslow and Knox, 1958; Gibbings, 1959; Kraemer, 1961; Lissaman, 1983; Simons, 1994; Lyon et al., 1997; Giguère and Selig, 1999; Gopalarathnam et al., 2003). Subsequent model wing studies with corrugated versus smooth model swift wings suggest that feather-like roughness reduces drag at Re=15,000, but not at higher *Re* (Lentink and de Kat, 2014). Because the flow field was not measured in the swift study, in contrast to the study of the 3D printed hummingbird wing (Elimelech and Ellington, 2013), it remains unclear how the boundary layer flow over bird wings responds to feather-induced roughness versus a smooth surface. Ideally, this would be studied across a range of angles of attack and Reynolds numbers that cover a bird's behavioral flight envelope. The swift is an ideal bird to study the effect of surface roughness, and compare with findings for hummingbirds, because swifts operate at similar low Re≈20,000 (*Re* ranges from 12,000 to 77,000; Lentink et al., 2007) and are closely related to hummingbirds (Videler, 2006; McGuire et al., 2014). However, in contrast to hummingbirds, which almost always flap their wings, swifts glide a substantial part of their lifetime (Videler et al., 2004; Lentink et al., 2007; Henningsson and Hedenström, 2011). This makes flow tunnel studies for swifts both biologically and aerodynamically representative. We used earlier surface roughness measurements of the common swift (*Apus apus*) hand wings (Lentink and de Kat, 2014) to 3D print model wings, and perform boundary layer flow measurements using very high-resolution snapshot particle image velocimetry (PIV). The experiments were carried out in a water tunnel at biologically relevant *Re* and α at which the swift is known to cruise energy efficiently with fully extended wings (Lentink et al., 2007; Henningsson and Hedenström, 2011). To determine the precise effect of surface roughness on flow separation, transition and reattachment over the airfoil of the swift wing, we compared a 3D printed wing with realistic feather roughness versus a smooth surface (Fig. 1).

RESULTS

To determine the effect of feather roughness on the boundary layer flow over a fully extended swift wing during cruise, we measured the flow field over model swift wings using PIV to compare the average velocity field, the vorticity fluctuations in instantaneous flow fields, detailed near-surface flow fields, and boundary layer velocity profiles. These differences were quantified using three

Journal of Experimental Biology (2015) 218, 3179-3191 doi:10.1242/jeb.121426

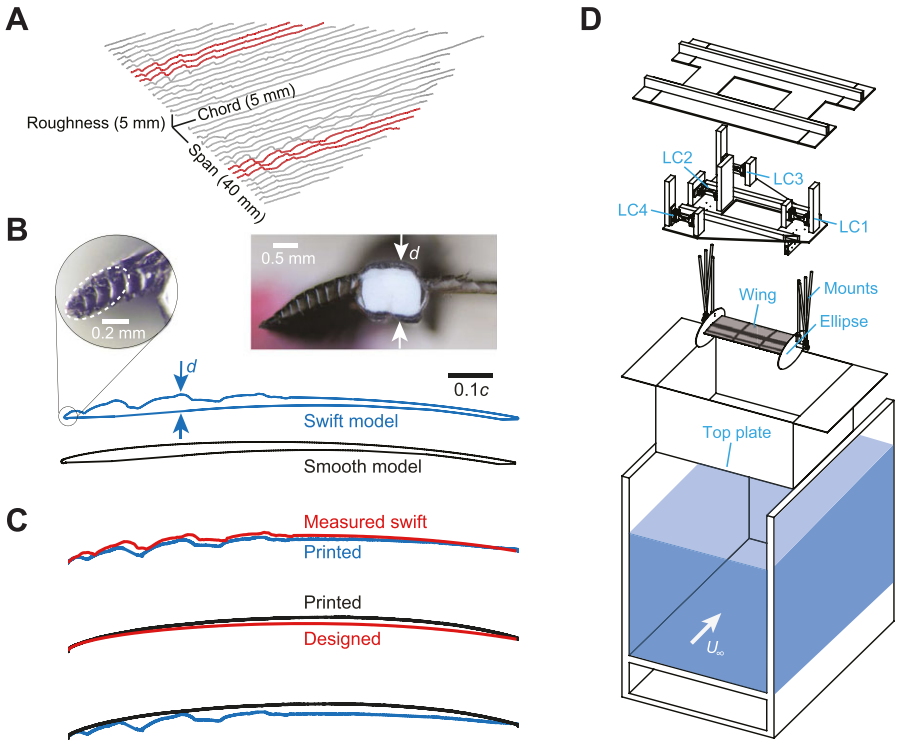

Fig. 1. Design of the 3D printed swift-like airfoil with a corrugated versus smooth surface. (A) Measured roughness profiles of a swift wing at 10 mm intervals show that the maximal roughness height occurs on the hand wing (three scan lines are indicated in red, left and right. The *x*- (chord), *y*- (roughness) and *z*-axis (span) are scale bars of the indicated length. (B) Rough versus smooth swift-like airfoil: the smooth airfoil is based on the average upper surface camber of the rough airfoil. The leading edge design of both airfoils is based on a microscopy image of the cross-section of the leading-edge primary feather of the swift hand wing. Airfoil thickness is based on primary feather rachis diameter (*d*). (C) Average upper surface profile of the swift hand wing (measured, red, versus 3D printed, blue) and smoothed profile (designed, red, versus 3D printed, black). Measured differences between CAD models and printed wings are due to the 3D printing process. The tiny protrusions at the leading and trailing edge are data-averaging artefacts and do not represent the surface. (D) Exploded view of the particle image velocimetry (PIV) and force measurement setup in a water tunnel with a 0.6×0.6×5.0 m test section. A top plate on the water surface suppresses the influence of surface waves, ellipse-shaped end plates reduce 3D effects, and load cells (LC) 1–4 provide force data. U_∞, free-stream velocity.

boundary layer parameters: boundary layer thickness δ_{99}, shape factor H and peak Reynolds stress along the chord length. To determine whether the changes in boundary flow dynamics changed glide performance, we measured lift and drag with load cells and calculated the lift-to-drag ratio, which indicates how far the swift can glide per meter height loss.

Flow separation zones in average flow fields

Averaged flow fields showed that wings with feather-like roughness generate attached flow across cruise Reynolds numbers (we tested $Re\approx$13,000 to 30,000) for both low and high geometric α (4.5, 9.0 and 13.5 deg). In contrast, the smooth surface promotes laminar separation bubbles that depend on α, and open trailing-edge separation bubbles that depend on *Re* (Fig. 2). Across all angles of attack, the flow over the corrugated airfoil recirculates in the valleys between the rachis, forming well-contained laminar separation bubbles. Aft of the most pronounced corrugation, the boundary layer remains attached all the way to the trailing edge for all Reynolds numbers and α tested (Fig. 2). The smooth surface, in contrast, provides no control over boundary layer development. At low α, the flow separates beyond the point of maximum height and forms a large open laminar separation bubble that connects to the wake (Fig. 2A). The open separation bubble grows with α at low *Re* up to 20,000, i.e. the cruise *Re* of swifts (Lentink et al., 2007), but much reduces at *Re* 24,000 and beyond, showing that the boundary layer dynamics on a smooth surface is very sensitive to *Re*. At maximal α, both the corrugated and smooth surface generate a thick boundary layer with isolated laminar separation bubbles near the leading edge. The open bubble on the smooth surface is relatively thin and similar for all *Re* tested, while the small bubbles on the rough surface remain contained in the surface roughness valleys.

Vorticity and velocity fluctuations in the boundary layer

The instantaneous vorticity fields for cruise Reynolds numbers show that patches of vorticity are shed from the roughness elements for moderate and high angles of attack (Fig. 3). Much smaller vorticity fluctuations are found on the smooth surface, and only in the region of the trailing edge where the flow separates at moderate angles of attack. For high angles of attack, both surfaces generate extensive vorticity fluctuations induced by the laminar separation bubble at the leading edge. The associated velocity fluctuations mix the low- and high-speed regions in the boundary layer (Fig. 4).

Laminar versus turbulent boundary layer development

To understand how the rough versus smooth surface influences boundary layer dynamics, we define standard boundary layer parameters in Fig. 5, and plot the average boundary layer profile development along the chord in Fig. 6. The unsteadiness in the boundary layer is quantified by plotting the standard deviation in the velocity profile. Comparison of the different treatments, rough versus smooth surface, low versus high α, and low versus high *Re*, show they have a pronounced effect on boundary layer development. As expected, a smooth surface, low angle of attack and low Reynolds number promote steady laminar flow. Remarkably, the boundary layer remains laminar over the rough surface for low α and *Re* despite a roughness height that is similar to the measured local boundary layer thickness (Fig. 6). The boundary layer thickness is affected by the roughness; it grows faster along the chord of the rough wing for low and moderate angles of attack (Fig. 7). The shape factor of the boundary layer profile, H, increases rapidly at the trailing edge of the smooth surface where large separation bubbles are formed (Fig. 8). This is expected as shape factors beyond 4 indicate boundary layer flow reversal (Drela, 2014). The enhanced mixing due to unsteady

Journal of Experimental Biology (2015) 218, 3179-3191 doi:10.1242/jeb.121426

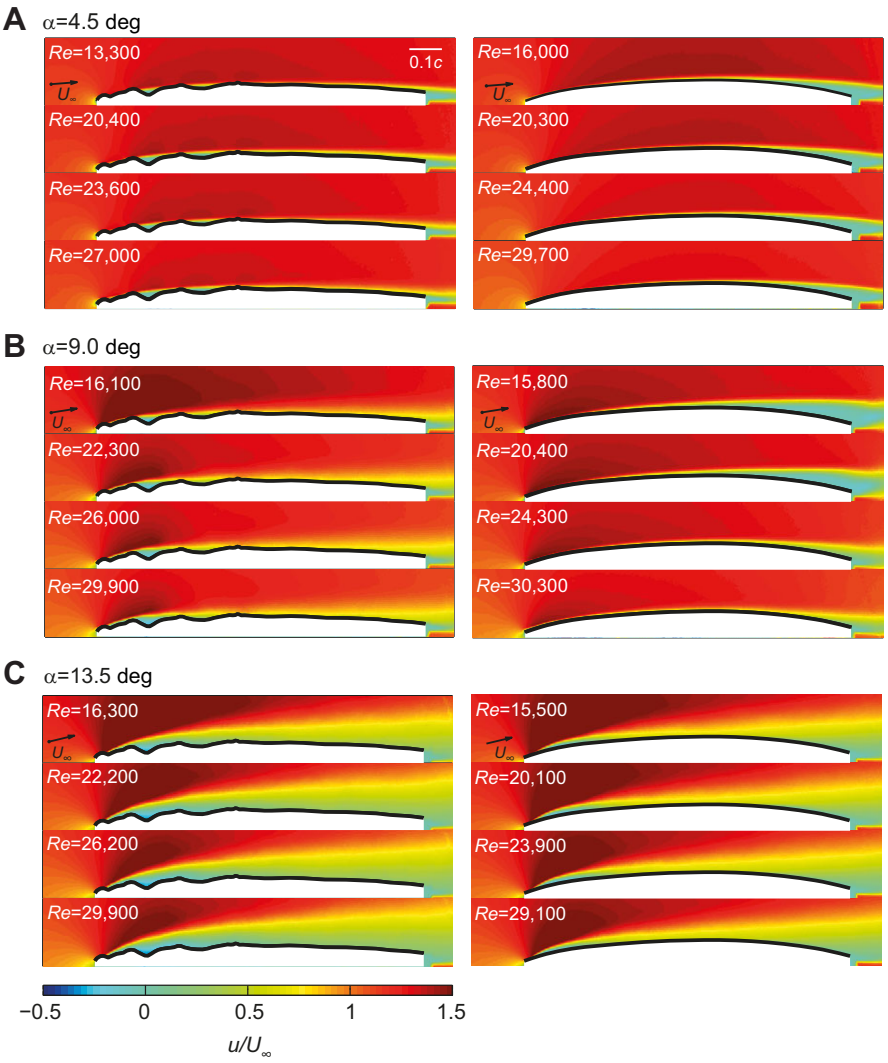

Fig. 2. Averaged flow fields for a swift-like airfoil with feather roughness versus a smooth surface as a function of Reynolds number *Re* and angle of attack α. (A) At α=4.5 deg, the flow over the rough airfoil (left) separates and recirculates in the valleys between the rachis bumps, but beyond the biggest bumps it remains attached till the trailing edge. The flow over the smooth airfoil (right) remains attached until about 70% chord length (*c*), after which the flow separates beyond the trailing edge. (B) At α=9.0 deg, the flow over the rough airfoil (left) also remains attached until the trailing edge. At low *Re*, the flow over the smooth airfoil (right) separates beyond about 50% chord length, but at high *Re* the flow separation is much reduced. (C) At α=13.5 deg, the flow over both the rough (left) and smooth (right) wing remains attached beyond a region near the leading edge where a laminar separation bubble is formed over both surface types. *u*, chordwise velocity

vorticity patches in the boundary layer enhances turbulent shear stress (Fig. 9; see 'PIV data analysis' in Materials and methods), also known as Reynolds stress (Drela, 2014). This Reynolds shear stress is mostly zero over the smooth surface up to moderate angles of attack, showing the flow is indeed laminar and separates laminar at the trailing edge. Similarly, the Reynolds shear stress remains zero over the rough surface for the lowest α and *Re*, but not beyond. The roughness elements cause high peaks in Reynolds shear stress, after which they converge to values of about 0.002 and 0.005 for low and moderate angle of attack. For the highest angle of attack tested, the Reynolds shear stress reaches similar peak values over both the smooth and rough wing, but beyond the peak, the rough surface sustains higher values in contrast to a stronger drop-off over the smooth surface.

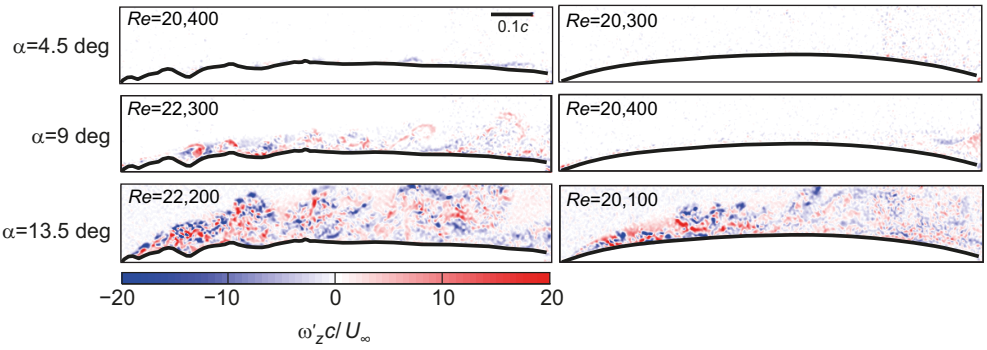

Fig. 3. Instantaneous vorticity plot based on the flow fluctuation field (*u*′, *v*′). Flow is laminar over the rough (left) and smooth (right) surface at low α at cruise *Re* of swifts. Comparison of rough and smooth surface effects for α=9.0 deg suggests that the surface roughness indeed forms a source of vorticity fluctuation in the shear layer. At α=13.5 deg, both the smooth and rough surfaces generate extensive vorticity fluctuations in the boundary layer, but qualitatively the vorticity fluctuations appear to be more broadly distributed for the rough surface. ω'_z, vorticity fluctuation.

Journal of Experimental Biology

Journal of Experimental Biology (2015) 218, 3179-3191 doi:10.1242/jeb.121426

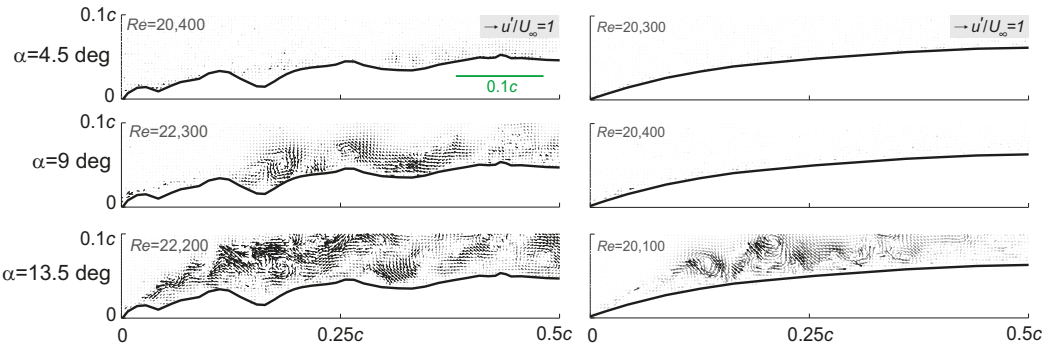

Fig. 4. Velocity vectors of the flow fluctuation field (u', v') confirm that surface roughness promotes boundary layer mixing. At α=4.5 deg, the flow over the rough surface (left) is essentially laminar, but at higher angles there is substantial unsteady boundary layer mixing. Boundary layer mixing due to fluctuations is not apparent for the smooth airfoil at α=4.5 and 9.0 deg (right). At 13.5 deg, the laminar separation bubble forms a source of unsteady fluctuations, which are qualitatively of lower intensity than those generated by the rough surface. Reference vector length, compared with the free-stream velocity, is provided in the gray box.

The influence of boundary layer dynamics on glide performance

The flow field measurements behind the airfoils were used to qualitatively evaluate the momentum deficit in the wake due to boundary layer deceleration over the airfoil (Fig. 10). Momentum deficit is an indicator of drag when measured far behind the airfoil where the wake is fully developed. Our near-wake measurements show that the flow separation over the smooth airfoil greatly increases

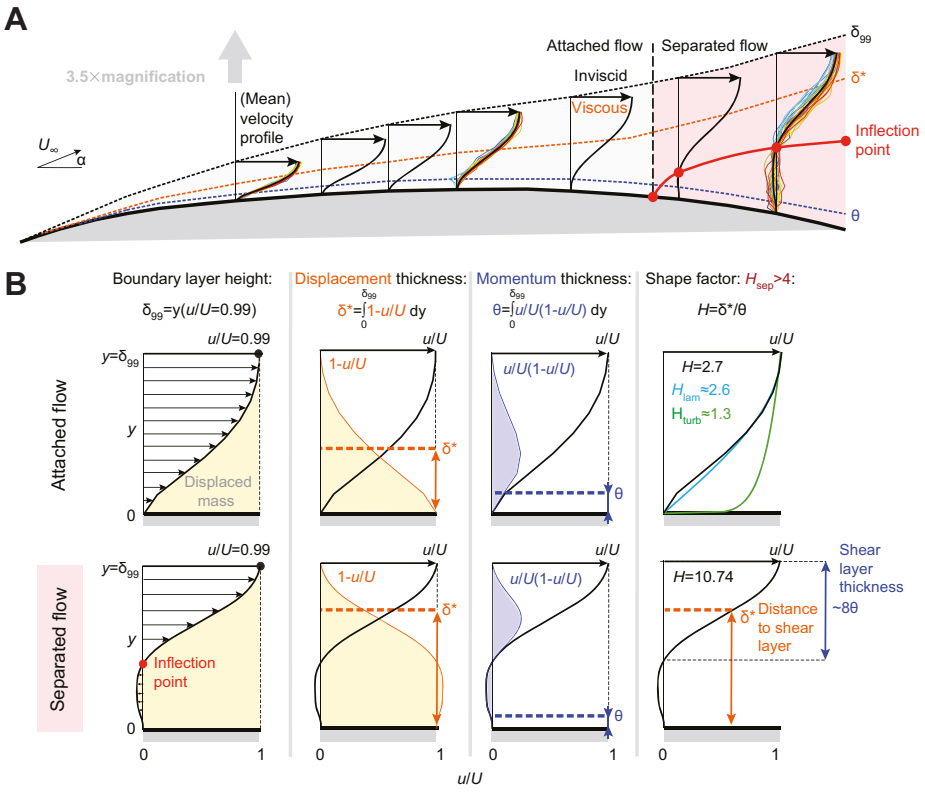

Fig. 5. Idealized boundary layer flow development over the smooth wing. This figure, intended to help introduce the boundary layer parameters used in Figs 6–8, and its explanations are adapted from White (1991) and Drela (2014). (A) Illustration of boundary layer flow over the smooth wing using average (black) and instantaneous (rainbow) flow profiles measured at α=9.0 deg and Re=20,400 (U_∞, free-stream velocity). The development of the boundary layer from the leading to trailing edge is characterized by the boundary layer thickness (δ_{99}, black dashed line), the displacement thickness (δ^*, orange dashed line), the momentum thickness (θ, blue dashed line) and the inflection points (red dots connected by a red line). For clarity, we magnified the vertical axis in the boundary layer by a factor of 3.5. (B) Graphical illustration of the integral boundary layer parameters that characterize boundary layer development, local laminar versus turbulent attached flow, and flow separation (Drela, 2014). Boundary layer height, δ_{99}, is the vertical position at which the flow reaches 99% of tangential velocity at the edge of the boundary layer (y, wall-normal location; u, chordwise velocity; U, tangential velocity at the edge of the boundary layer). Displacement thickness, δ^*, is a measure for how far the main flow is pushed away from the surface. Momentum thickness, θ, is a measure for how far the momentum of the main flow is pushed away from the surface. Shape factor, H, is the ratio of displacement and momentum thickness, and characterizes the shape of the velocity profile for attached turbulent (H_{turb}≈1.3) and laminar (H_{lam}≈2.6) flow. For separated flows, the corresponding shape factor is H_{sep}>4 and δ^* is a measure for how far the shear layer is separated from the wall, while the thickness of the separated shear layer can be estimated as 8θ (Drela, 2014).

Journal of Experimental Biology

Journal of Experimental Biology (2015) 218, 3179-3191 doi:10.1242/jeb.121426

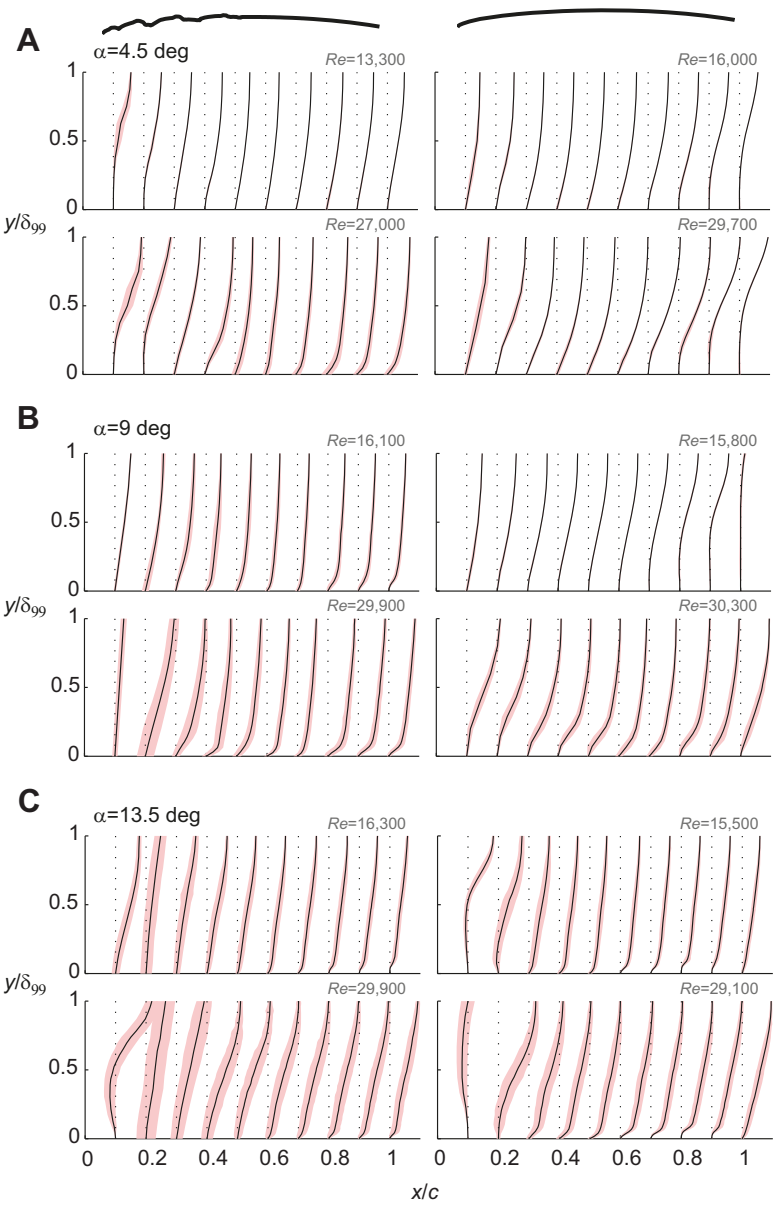

Fig. 6. Boundary layer separation is reduced by roughness, high Reynolds number and high angle of attack. Boundary layer thickness, δ_{99}, is defined based on when the velocity reaches 99% of the tangential velocity at the edge of the boundary layer. Solid lines indicate the average velocity profile for different chord positions *x*/*c*, whereas the colored area indicates boundary layer profile standard deviation. An inflected boundary layer profile indicates flow separation, which can be reduced by flow fluctuations that mix the boundary layer, indicated by large standard deviation. Boundary layer profiles are shown for rough (left) versus smooth (right) surface at three different angles of attack, α=4.5 deg (A), 9.0 deg (B) and 13.5 deg (C), at the minimum versus maximum Reynolds number tested for the rough and smooth surface. The non-zero velocity standard deviation at the surface of the pronounced corrugation is due to PIV limitations.

the momentum deficit behind the airfoil at intermediate α and low *Re*. Under other conditions, the momentum deficit generated by the rough versus smooth airfoil is more similar. The effect of these and other flow differences on performance was evaluated quantitatively with lift and drag force measurements using load cells (Fig. 1). The comparison of drag coefficients and lift-to-drag ratio (glide ratio; Fig. 11) shows that the glide ratio obtained with a swift-like rough versus engineering-like smooth surface is essentially equivalent within the precision of our drag measurements.

DISCUSSION

To determine the effect of feather roughness on the boundary layer flow over a fully extended swift wing during cruise and glide performance, we contrasted high-resolution flow fields and force measurements. We found that feather roughness makes the boundary layer flow robust to laminar flow separation across Reynolds numbers – improving the aerodynamic robustness of the swift hand wing. Remarkably, this significant flow improvement has only a small effect on glide performance in terms of drag or lift-to-drag ratio.

Feather roughness suppresses Reynolds number and angle-of-attack effects

The measured flow fields show that wings with feather-like roughness generate attached flow across cruise Reynolds numbers (we tested *Re*≈13,000 to 30,000) for both low and high geometric α (4.5, 9.0 and 13.5 deg). In contrast, flow over the smooth surface experiences massive laminar flow separation, which depends on α and *Re* in a non-linear fashion. The surface roughness thus effectively controls the dynamics of laminar separation bubble formation throughout the glide envelope of the swift. The upper surface corrugation of swift hand wings resembles the corrugation of dragonfly airfoils, but is concentrated towards the leading edge and has a 5–10 times smaller amplitude (Kesel, 2000; Jongerius and Lentink, 2010; Lentink and de Kat, 2014). Corrugated dragonfly airfoils also generate laminar separation bubbles in the valleys formed by the corrugation (Rees, 1975a; Buckholz, 1986; Lentink and Gerritsma, 2003; Vargas and Mittal, 2004; Kim et al., 2009; Levy and Seifert, 2009, 2010; Murphy and Hu, 2010; Hord and Liang, 2012); such effects of corrugation have not been demonstrated before in birds (Elimelech and Ellington, 2013).

Journal of Experimental Biology (2015) 218, 3179-3191 doi:10.1242/jeb.121426

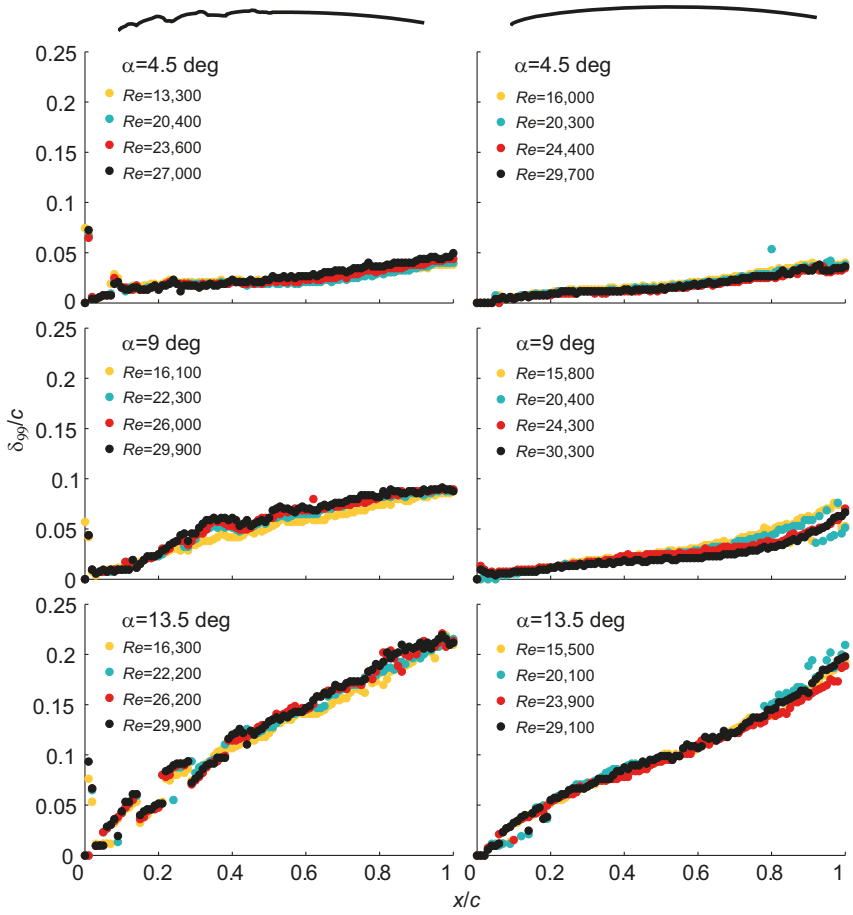

Fig. 7. Boundary layer thickness (as a proportion of chord) over the rough and smooth surface is similar to the swift wing roughness. Boundary layer thickness, δ_{99}, increases with relative chord position *x*/*c* and is not very sensitive to Reynolds number, instead depending primarily on α and roughness. At α=4.5 and 9.0 deg, δ_{99} is close to 0.02 (2%) chord length for the rough (left) and smooth (right) surface. At α=9.0 deg, the boundary layer over the rough surface quickly increases in thickness beyond *x*/*c*=0.2 as a result of mixing induced by the surface roughness (Fig. 4). The surface roughness of the swift wing is thus equivalent to boundary layer thickness over the smooth airfoil (at the location of this roughness) and over the rough airfoil at α=4.5 deg and up to *x*/*c*=0.2 for α=9.0 deg.

The similarity in laminar separation bubbles found on dragonfly and swift wings is remarkable, considering dragonflies operate at *Re* below 10,000 for which experiments show the boundary layer flow remains laminar (Levy and Seifert, 2009), whereas the flow over hummingbird wings at *Re*=15,000 and α=10 deg can be turbulent in the separated shear layer above the surface (Elimelech and Ellington, 2013). But it is still not entirely clear to what extent boundary layers are either laminar or turbulent over the surface of bird wings.

The boundary layer is laminar over rough swift wings at low but not high α and *Re*

Snapshots of flow fluctuations in the boundary layer, and the averaged boundary layer profiles, show that the corrugated and smooth surfaces generate laminar boundary layers at low α. At intermediate α, the corrugation generates turbulent vortex structures that greatly enhance boundary layer mixing and prevent flow separation, whereas the smooth surface generates a laminar boundary layer that separates at low *Re*. Flow separation is prevented at high α, because both the smooth and corrugated surface generate similar turbulent structures that originate from the leading edge region. In this region the flow appears to transition into turbulence as a result of shear layer instability over the laminar separation bubble (Fig. 3). We further studied this by zooming in on our high-resolution flow data (Fig. 4), which suggested that the function of surface corrugation is to generate clusters of small vortices that greatly enhance boundary layer mixing (Figs 3, 4). The smooth surface does not promote such mixing at low α; however, it does at high α through the shear layer instability over the laminar separation bubble near the leading edge of the wing. This induces strong flow fluctuations that mix the boundary layer to a similar extent to that found for the corrugated surface (Fig. 4). To better characterize under which conditions the flow remains laminar, we plotted both the boundary layer velocity profile and its standard deviation (Fig. 6). The insignificant standard deviation of the velocity at low *Re* demonstrates that the flow is indeed laminar over both the smooth and corrugated wing at α=4.5 deg. This supports earlier findings of laminar flow over prepared swift wings in a wind tunnel, despite their roughness height of up to 2% chord length (Lentink and de Kat, 2014). The smooth surface also generates a laminar boundary layer; however, it features pronounced flow separation beyond 60% chord at all *Re* tested for α=4.5 deg. In contrast, the corrugated surface generates well-contained laminar separation bubbles above the corrugated surface near the leading edge, and not beyond. Similar to findings for prepared swift wings, we also found that the extent of laminar flow over the rough wing depends on both *Re* and α. The velocity fluctuations at α=9 and 13.5 deg (Fig. 4) show that the corrugated surface induces a standard deviation – due to the vortices it generates (Fig. 3) – in the velocity profile (Fig. 6). At high *Re*, the smooth surface also generates such vortices (Fig. 3) and standard deviation, reducing flow separation (Fig. 6). Across α and *Re*, the corrugated surface successfully locks the extent of flow separation to the corrugated region. In contrast, the smooth surface generates large open separation bubbles near the trailing edge at low α and smaller separation bubbles near both the leading and trailing edge at high α. This further suggests that wing corrugation helps to control the extent of flow separation over the surface. The extensive laminar flow over the corrugated surface for α=4.5 deg and *Re*=13,300, but not for α=9 deg and *Re*=16,300 (Fig. 6), suggests that the turbulent flow in a

Journal of Experimental Biology (2015) 218, 3179-3191 doi:10.1242/jeb.121426

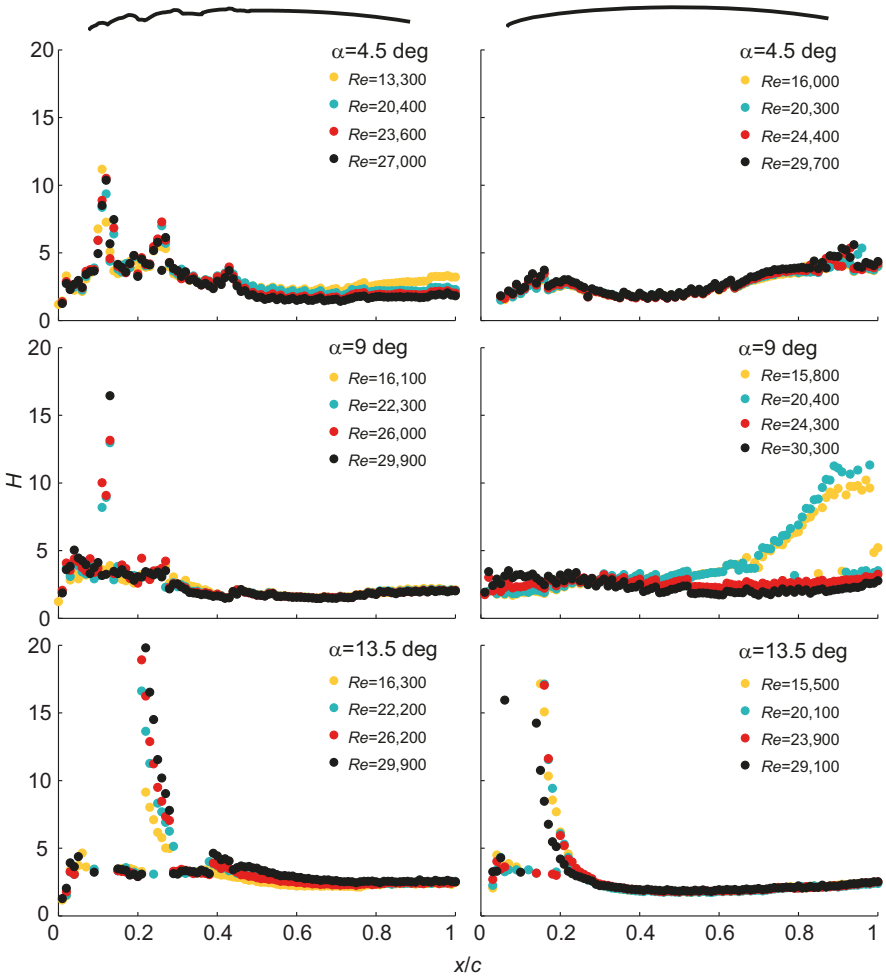

Fig. 8. Shape-factor development over the rough surface is similar across *Re* and α, in contrast to the smooth surface. Boundary layer shape factors, *H*, beyond 4 highlight areas where the boundary layer separates. Only the peak values of the shape factor vary substantially with *Re* over the rough surface (left): they shift backward at higher α. In contrast, the shape factor development over the smooth surface (right) is strongly Reynolds number dependent at α=9.0 deg, with high values that confirm the flow is separated. Shape factor development varies with α.

separated shear layer above a 3D printed hummingbird wing reported by Elimelech and Ellington (2013) is likely due to the high angle of attack. We note, however, that the shear layer over our model swift wing re-attaches immediately behind the corrugated area for α=4.5–13.5 deg. We think this enhanced performance of the printed swift versus hummingbird wing can be attributed to the additional care we have taken in measuring and replicating a nose radius that is representative for the leading primary feather of the swift wing (Fig. 1). Based on recently published aerodynamic measurements on prepared hummingbird wings (Kruyt et al., 2014), we know the leading edge of a hummingbird hand wing (*Calypte anna*) is thinner than the 3D printed hummingbird wing of Elimelech and Ellington (2013). The leading edge shape of the avian hand wing matters for aerodynamic performance, as reported earlier for swift wing models, which need a sharp leading edge to generate a leading edge vortex (Videler et al., 2004; Videler, 2006), and for gliding barn owls, for which the serration of their leading-edge primary feather helps reduce flow separation (Winzen et al., 2014).

Feather roughness keeps trailing-edge flow separation under control by forcing turbulence

Boundary layer height measurements show that the roughness height of a swift hand wing is indeed equivalent to boundary layer thickness over a smooth surface under similar conditions (Fig. 7). The boundary layer shape factor, *H*, confirms that the boundary layer over the smooth airfoil is fully separated at low and intermediate α, highlighted by shape factors beyond *H*=4 (Drela, 2014), with the exception of intermediate α at high *Re*, which shows a dramatic divide due to *Re* (Fig. 8). In contrast, the corrugated surface generates boundary layer profiles that are the same across Reynolds number. Shape factor *H* peaks at maximal α for all *Re* on both surfaces, indicating separated flow at the leading edge. To better quantify the state of the boundary layer, we computed the development of the Reynolds number based on momentum thickness, Re_θ, over the corrugated surface as a function of α. For low α, Re_θ reaches values of about 71–175 at the trailing edge of the corrugated wing for increasing *Re*. For intermediate α, Re_θ ranges from 194 to 384, and for the highest α from 566 to 1061. The minimum Re_θ value for a sustained turbulent boundary layer is 320 according to Preston (1958); this supports our interpretation that the boundary layer is laminar at low α and *Re* and reaches a transitional or turbulent state at higher α and *Re*.

Reynolds shear stress plots indeed confirm laminar flow at low α, which transitions at high *Re* for the corrugated wing. At intermediate α, the Reynolds shear stress distributions become approximately constant starting at values beyond 0.02 and converging to values close to 0.005. Very similar values and trends were found in the region behind a zigzag roughness strip (Elsinga and Westerweel, 2012) and the order of magnitude corresponds with turbulent flow conditions over a flat plate (Klebanoff, 1955; Erm and Joubert, 1991; Ducros et al., 1996; de Graaff and Eaton, 2000). On the smooth surface the Reynolds shear stress values and distribution found are comparable to those found for separation bubbles on low Reynolds number airfoils (Yuan et al.,

Journal of Experimental Biology (2015) 218, 3179-3191 doi:10.1242/jeb.121426

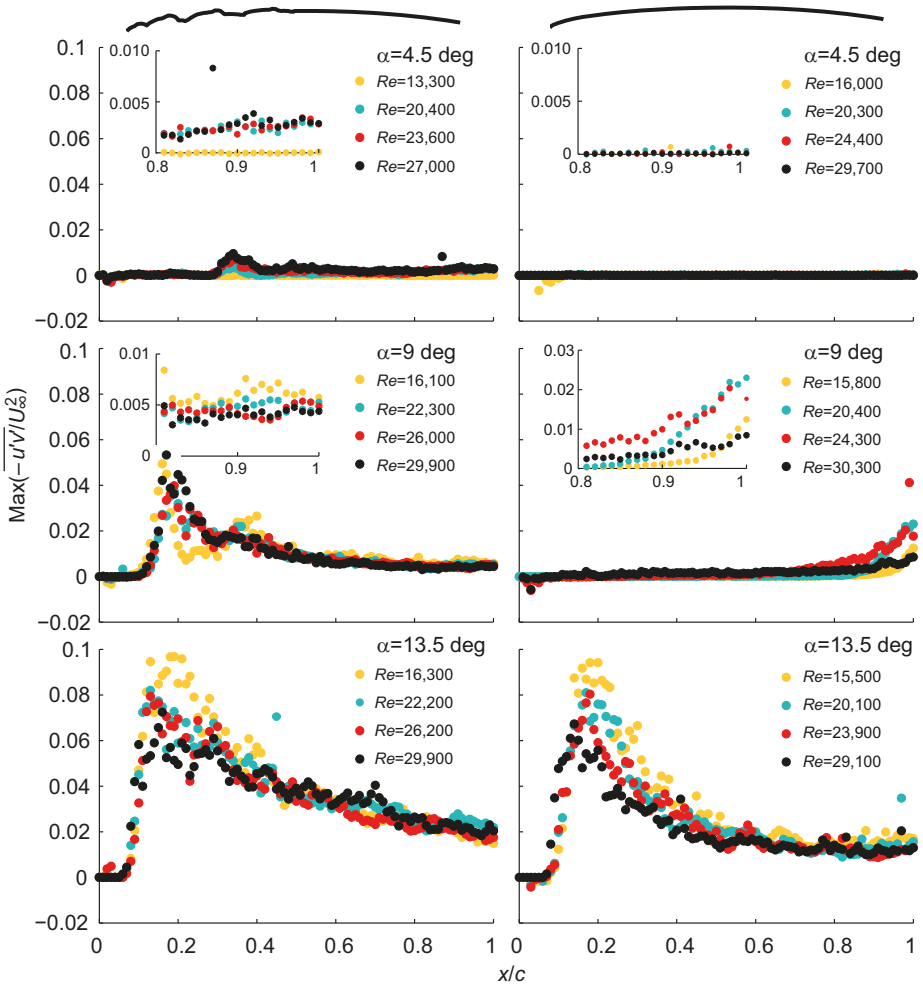

Fig. 9. Swift feather roughness generates significant Reynolds shear stresses of the order of 0.01 and up, a signature of transitional turbulent flow. At α=9.0 and 13.5 deg, the roughness generates vortices (Fig. 4) that strongly enhance mixing and thus generate Reynolds shear stress. The smooth (right) and rough (left) surface only generate similar Reynolds shear stress at α=13.5 deg, when the shear layer separates on the smooth airfoil and becomes turbulent above a laminar separation bubble (Figs 2–4 and 7). The chordwise Reynolds shear stress production is weakly dependent on Reynolds number, except for the rough surface at α=4.5 deg, where it locally jumps from zero to non-zero when *Re* increases from 13,300 to 20,400.

2005; Lian and Shyy, 2007). At high α, both surfaces generate high peak Reynolds stress values that indicate turbulent flow. Turbulence at low Reynolds numbers, however, more likely represents a state of transitional turbulence without a pronounced −5/3 spectrum (Erm and Joubert, 1991; Mydlarski and Warhaft, 1996); further studies are needed to test this hypothesis. Finally, we compared the wake velocity deficit profile to understand how surface roughness affects airfoil drag. The profiles confirm that the smooth surface airfoil is Reynolds sensitive, whereas the rough surface is not. Otherwise, the wake profiles are relatively similar, which suggests that profile drag is relatively similar beyond the Reynolds effect because of flow separation on the smooth surface at α=9.0 deg. The wake profiles are measured at 5% chord length behind the trailing edge and are, therefore, not fully developed. Thus, small differences in wake profiles cannot be interpreted directly in terms of profile drag (Spedding and Hedenström, 2009).

Influence of wing corrugation on flight performance and structural function

Earlier studies of the corrugated airfoils of dragonfly wings have shown they function well at low Reynolds numbers in terms of aerodynamic and structural performance. The corrugation improves the structural stiffness of the wing (Rees, 1975b; Kesel, 2000). Similarly, elevated rachis height will improve the stiffness of bird hand wings (Lentink and de Kat, 2014), a feature that is thought to be an important prerequisite for the flight of protobirds (Nudds and Dyke, 2010). Precise lift and drag measurements on model swift wings in a wind tunnel showed that surface roughness due to rachis height results in either equivalent or better aerodynamic performance than smooth wings, in particular at the cruise Reynolds number of swifts (Lentink and de Kat, 2014). The present force measurements on model swift wings in the water tunnel support this finding: the rough and smooth wings generate equivalent drag, and equivalent lift-to-drag ratio (Fig. 11), to within our measurement uncertainties due to Reynolds differences and load cell resolution limits. Further aerodynamic analysis is needed to understand why performance differences are small. The fact, however, that such rough wings perform equivalent to smooth wings, similar to findings for barn owls (Winzen et al., 2014), is an important insight specific for low Reynolds numbers. Our detailed high-resolution PIV study supports earlier qualitative measurements showing that the boundary layer stays laminar over rough swift wings at low angles of attack, a remarkable feat for 2% rough wings, but becomes turbulent at high angles of attack. Turbulence prevents laminar separation development over the rough wing, which gives it more reliable aerodynamic qualities, in contrast to the smooth surface. The equivalent glide performance of smooth and very rough airfoils is specific to the extremely low Reynolds numbers of about 20,000 at which swifts glide; at the higher Reynolds numbers of albatrosses, smooth wings should outperform rough, aerodynamically unsophisticated, wings. The demonstrated insensitivity of glide performance to surface roughness at low Reynolds numbers might have provided small protobirds with an evolutionary window to high glide performance (Lentink and de

Journal of Experimental Biology (2015) 218, 3179-3191 doi:10.1242/jeb.121426

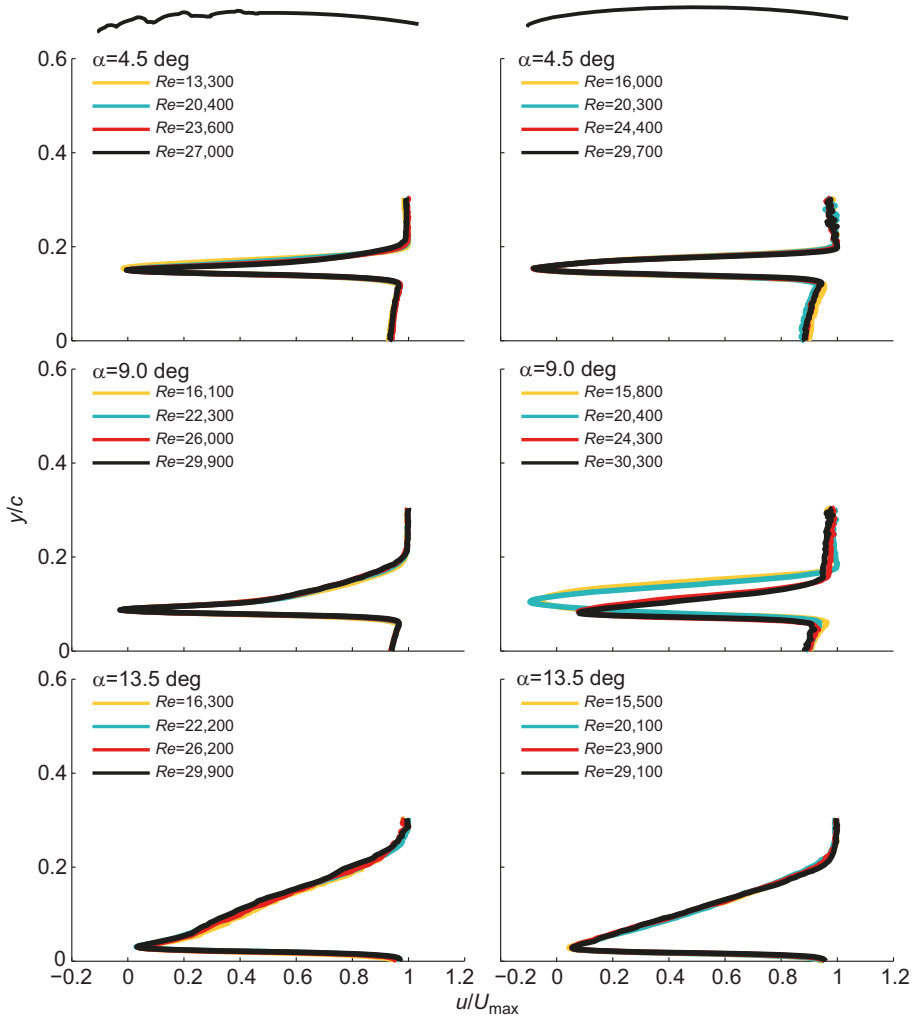

Fig. 10. Wake velocity deficit profiles at *x*/*c*=1.05 (5% behind the trailing edge) show the wake generated by the rough surface (left) is similar across *Re*. The boundary layer over the upper surface dictates the development of the upper part of the wake profile, which depends on α. The wake profile behind the smooth airfoil is *Re* sensitive at α=9.0 deg because of flow separation over the smooth surface (right) (Fig. 5).

Kat, 2014). Simultaneously, the higher allowable wing roughness enabled the rachis to be thicker, which might have been a critical step towards high glide performance in protobirds, which needed this rachis height to lift their body weight (Nudds and Dyke, 2010). In modern birds, elevated rachis height helps withstand higher wing loading (G-loading) during turning maneuvers. Similarly, the finding that high wing roughness is allowable at the Reynolds numbers of swifts will help set more reasonable manufacturing tolerances on the wings of hand-sized micro air vehicles. Future studies might show how optimal wing roughness varies as a function of ecotype and Reynolds number across birds, ranging from hummingbirds to albatrosses.

MATERIALS AND METHODS

Water tunnel

The experiments with the wings were carried out in a water tunnel with a test section that was 60 cm wide, 60 cm high and 500 cm long, and a flow speed that could be controlled up to 1 m s^{-1} (Schröder et al., 2011; Harleman, 2012). The turbulence level of the free-stream velocity was below 0.5% at a free-stream velocity of 0.53 m s^{-1}; this value contains both the free-stream turbulence and the measurement noise. As we took measurements at somewhat lower speeds of roughly 0.1 and 0.2 m s^{-1}, we conservatively estimated the turbulence level to be below 1%. For natural boundary layer transition over a flat plate, the present free-stream turbulence levels (<1%) are not considered to have a significant effect (e.g. Brandt et al., 2004; Fransson et al., 2005). The test section of the water tunnel was open at the upper side; therefore, to minimize the effect of surface waves on the flow over the model wing, a top plate that spanned the length of the test section was slightly submerged below the water surface.

Model swift wing design

Our 3D printed, rough versus smooth, model swift wings are based on surface roughness measurements of actual fully extended swift wings. The upper surface shape was measured at 37 spanwise locations with 10 mm spanwise spacing using a custom-designed 3D laser line scan set-up (Lentink and de Kat, 2014). The hand wings had a pronounced surface roughness of up to about 2% chord at spanwise stations 110, 120 and 130 mm distally on the left and right wing. We averaged the surface roughness profile of these six stations using custom-written MATLAB software (MathWorks R2013b). This software identifies and preserves the bumps formed by the rachides so that the average shape is representative of the upper surface. The lower surface was approximated with a smooth cambered surface that follows the upper surface. We approximated the leading edge of the wing with an ellipse corroborated from stereomicroscope images (Olympus stereo microscope, SZX9) of the leading edge cross-section (Fig. 1). Considering the thinness of distal feather morphology, we selected a sharp trailing edge (also typical for airfoils). The overall thickness of the model wing was based on the maximal rachis thickness of the hand wing, which also defines the smooth lower surface design. We used this 2D profile to extrude a 3D rectangular planform wing with constant chord length using SOLIDWORKS (Dassault Systèmes 2012). The smooth model had the same overall geometry. We optimized wing dimension to fit in the water tunnel test section, to achieve swift Reynolds numbers, and to enable accurate boundary layer flow measurement using high-resolution PIV.

Journal of Experimental Biology (2015) 218, 3179-3191 doi:10.1242/jeb.121426

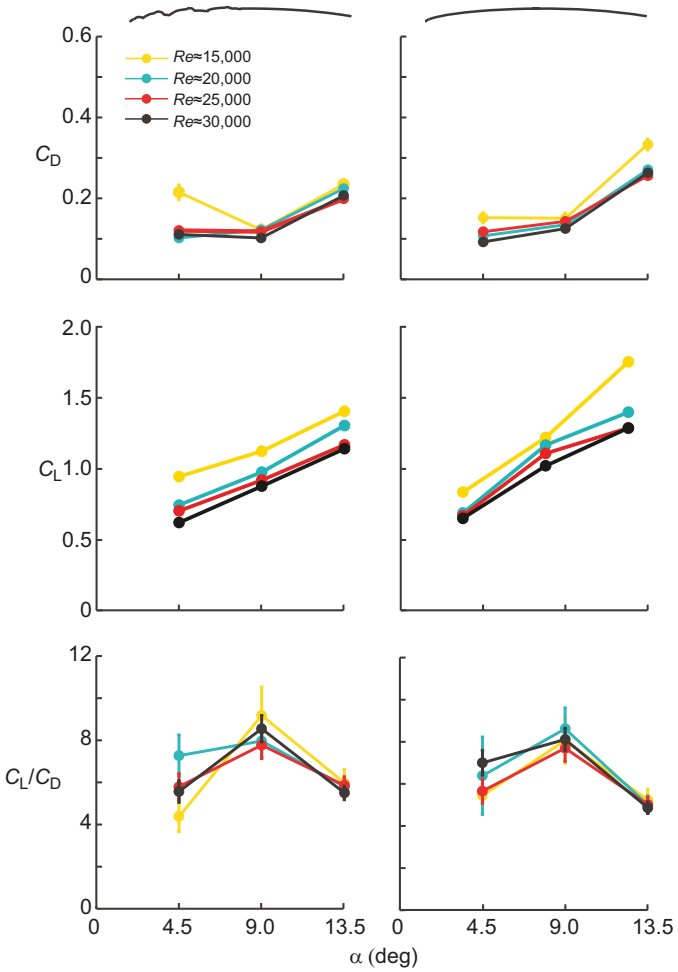

Fig. 11. Drag and lift coefficients (C_D and C_L) based on load cell measurements show surface texture has a small effect on drag and glide ratio. The drag measurements show that drag is weakly dependent on surface texture. Because the Reynolds number varies between the rough (left) and smooth (right) surface measurement (e.g. at α=4.5 deg, we compare *Re*=13,300 for the smooth surface versus *Re*=16,000 for the rough surface), we cannot interpret the small differences as *Re* is not strongly controlled for and minimal drag measurement is not very precise. Whereas differences in lift are more pronounced, the glide ratio calculations based on the lift and drag force measured with the load cells further suggest that surface roughness has a limited effect on glide performance.

The resulting wing had a 36 cm wingspan and 15 cm chord length, and was built up by three sections that spanned 12 cm each. To reduce 3D flow effects, we attached a 2 mm thin elliptical endplate to each wing tip (Mueller, 1999), and performed PIV measurements at the centerline of the wing.

Model swift wing manufacture

We designed and 3D printed (Projet 3500 HD Max) the three wing segments using a transparent plastic (VISIJET EX 200) with a resolution of 32 µm (layer thickness). To minimize deformations of individual wing elements due to melt-off of wax that supports the 3D printed structure, the models were heated in water at 60°C and clamped down during cooling. To improve chordwise stiffness and shape, we added thin ribs on the lower side of the wing with a spacing of 4 cm such that there was no rib on the lower surface at the centerline where we performed the PIV measurements. At the location of the model rachis, small holes remained in the 3D printed structure that we used to connect the three wing segments with stainless steel rods (1–2 mm diameter), glued in place with epoxy (Scotch Well DP810). We measured the cross-section of the assembled rough and smooth wing in the PIV laser sheet to compare it with the computer-aided design (CAD) model (Fig. 1): the rough model had about 1% less camber, and the smooth model had about 1.5% more camber than designed.

Reynolds number, geometric angle of attack and PIV

We selected combinations of *Re* (roughly 15,000–30,000; step size 5000) and α (geometric; 4.5, 9.0 and 13.5 deg) that are representative for swifts gliding at high efficiency (Lentink et al., 2007). Here, the Reynolds number is defined as $Re=\rho U_\infty c/\mu$, where ρ is the density and μ is the dynamic viscosity. The boundary layer flow over the model wings was measured using a PIV system consisting of three 16 megapixel cameras (Imager LX 16 Mpix, LaVision) positioned side by side in streamwise direction, imaging optics (Nikon AF Micro-Nikkor 105 mm f/2.8D, f=105 mm set at f 5.6), and a pulsed laser (Quanta ray Nd:YAG, Spectra Physics; 200 mJ pulse^{-1}, 4.2 Hz). The fields of view of the three high-resolution cameras spanned the entire chord length (150 mm) over the upper surface. The tracer particles (hollow microspheres, Sphericel; 10 µm in diameter) were illuminated within the laser sheet (about 1–2 mm thick), which spanned the free-stream and cross-stream direction. Within the sheet, light was directed at a shallow angle with the model surface, to minimize surface reflections, while avoiding shadows in between roughness valleys. Calibration of the setup was carried out with a 3D printed calibration plate positioned in the chordwise direction. The calibration error was about 1 pixel or 0.0017 mm. The time delay between laser pulses was selected to resolve the velocity gradient of the slower inner boundary layer, resulting in a free-stream particle displacement of about 10 pixels. The cross-correlation of the particle images was carried out in DaVis (LaVision 2013) using a multi-grid method and three iterative steps with 50% overlap for 300 image pairs to compute the ensemble average. The final interrogation window size was 32×32 pixels (0.56×0.56 mm^2). The estimated displacement error was about 0.1–0.2 pixels (Adrian and Westerweel, 2010) or 0.0017–0.0034 mm. Finally, we used the results of the load cells to approximate the angle of attack at which the wings obtain zero lift, which is −6.6 deg (±1.8 deg s.d.) for the rough wing and −3.1 deg (±1.4 deg s.d.) for the smooth wing (averaged over *Re* and fitted based on all three α). This facilitates coarse comparison with earlier measurements on prepared swift wings (Lentink et al., 2007; Lentink and de Kat, 2014).

PIV data analysis

The flow fields obtained with the PIV setup were processed to determine the average flow field, vorticity field and Reynolds shear stress distribution over the model wings. The average velocity field was computed using 60, 120, 180 and 240 instantaneous flow fields in order to determine how many fields should be taken to get a converged average; we found 180 to be sufficient. To assure convergence, we acquired and processed 300 flow fields for each experiment. The average velocity field was computed using 60,120,180 and 240 instantaneous flow fields in order to determine how many fields should be taken to get a converged average. We found 180 to be sufficient, but to assure convergence, we acquired and processed 300 flow fields for each experiment. To determine the presence of vortices in the flow, we subtracted the mean velocity field from an instantaneous velocity field to obtain the velocity fluctuation field (u',v') and calculated the associated fluctuations in the vorticity field as follows: $\omega'_z=(\partial v'/\partial x)-(\partial u'/\partial y)$.

To evaluate the laminar versus turbulent state of the boundary layer, we calculated the boundary layer thickness, shape factor and Reynolds shear stress. A limitation of the first two measures is that the theoretical values associated with turbulent flow are only known for the boundary layer on a flat plate at higher Reynolds numbers. In comparison, the calculation of Reynolds shear stress, $\overline{u'v'}$, provides better contrast, because this stress is straightforward to calculate and is known to be significant in transitional and turbulent boundary layers. For a laminar boundary layer, the Reynolds shear stress will be very close to zero and, for the canonical fully developed turbulent boundary layer, typically normalized values are around 0.001–0.002 (Klebanoff, 1955; Erm and Joubert, 1991; Ducros et al., 1996; de

Graaff and Eaton, 2000). For comparison between experiments, we selected the maximum Reynolds shear stress at each chordwise position, within the boundary layer height, to assess the local turbulence level along the wing chord. Next, the boundary layer thickness (δ_{99}) and the shape factor (H) were determined along the entire chord in $0.01c$ steps (where c is the chord) (Fig. 5).

Load cell analysis

Lift and drag forces were measured with a configuration of four linear load cells (EP2 Scaime), which have a capacity of 20 N and accuracy of 0.02 N (Fig. 1). Drag and lift calibrations were carried out by applying known loads in 0.5 kg steps over the full lift and drag range of the cells. A linear fit gave RMSE (root mean square error) values of 0.07 and 0.13 N for the lift and drag, respectively. The data showed there was negligible cross-talk between the load cells. In order to extract the forces attributed to the model, forces created by the mounting system and endplates were measured independently for all angles of attack and velocities and corrected for. Forces for each angle of attack and Reynolds number were sampled at 1000 Hz and averaged over about 2 min of data. Based on the lift (L) and drag (D) forces, we calculated the corresponding dimensionless force coefficients as follows:

$$C_{\mathrm{D}} = \frac{D}{(1/2)\rho U_{\infty}^{2} sc},$$

$$C_{\mathrm{L}} = \frac{L}{(1/2)\rho U_{\infty}^{2} sc},$$

where s is the span and c is the chord length of the wing in meters, ρ is the density of water and U_{∞} is the free-stream velocity. The uncertainty calculation combined the standard deviation of the force measurements with and without the model. At low velocities, the magnitude of the drag forces was about 0.1 N, which led to relatively large uncertainties in the C_{D} coefficients and $C_{\mathrm{L}}/C_{\mathrm{D}}$ ratios, much larger than those in an earlier study (Lentink and de Kat, 2014). We therefore consider the earlier published wind tunnel force measurements more precise, whereas the present flow analysis is more detailed and sophisticated. Regardless, both studies are supportive of the performance conclusions based on the less precise force data presented here.

Competing interests

The authors declare no competing or financial interests.

Author contributions

E.v.B. performed the experiments. E.v.B., R.d.K., G.E. and D.L. conceived and designed the experiments, analyzed data and wrote the paper.

Funding

This research received no specific grant from any funding agency in the public, commercial or not-for-profit sectors. R.d.K. is supported by a Leverhulme Early Career Fellowship.

References

Adrian, R. J. and Westerweel, J. (2010). *Particle Image Velocimetry*. Cambridge: Cambridge University Press.
Azuma, A. (2006). *The Biokinetics of Flying and Swimming*. Reston, VA: American Institute of Aeronautics and Astronautics.
Bechert, D. W., Bruse, M., Hage, W. and Meyer, R. (1997). Biological surfaces and their technological application – laboratory and flight experiments on drag reduction and separation control. *28th Fluid dynamics conference*, Snowmass Village, CO: AIAA Meeting Papers.
Bechert, D. W., Bruse, M., Hage, W. and Meyer, R. (2000). Fluid mechanics of biological surfaces and their technological application. *Naturwissenschaften* **87**, 157-171.
Brandt, L., Schlatter, P. and Henningson, D. S. (2004). Transition in boundary layers subject to free-stream turbulence. *J. Fluid Mech.* **517**, 167-198.
Braslow, A. L. and Knox, E. C. (1958). *Simplified Method for Determination of Critical Height of Distributed Roughness Particles for Boundary Layer Transition at Mach numbers from 0 to 5 (Technical Note 463)*. Washington: NACA.
Buckholz, R. H. (1986). The functional role of wing corrugations in living systems. *J. Fluid. Eng.* **108**, 93-97.
de Graaff, D. B. and Eaton, J. K. (2000). Reynolds-number scaling of the flat-plate turbulent boundary layer. *J. Fluid Mech.* **422**, 319-346.
Dean, B. and Bhushan, B. (2010). Shark-skin surfaces for fluid-drag reduction in turbulent flow: a review. *Philos. Trans. A Math. Phys. Eng. Sci.* **368**, 4775-4806.
Drela, M. (2014). *Flight Vehicle Aerodynamics*. Cambridge, MA: MIT Press.
Ducros, F., Comte, P. and Lesieur, M. (1996). Large-eddy simulation of transition to turbulence in a boundary layer developing spatially over a flat plate. *J. Fluid Mech.* **326**, 1-36.
Elimelech, Y. and Ellington, C. P. (2013). Analysis of the transitional flow field over a fixed hummingbird wing. *J. Exp. Biol.* **216**, 303-318.
Elsinga, G. E. and Westerweel, J. (2012). Tomographic-PIV measurement of the flow around a zigzag boundary layer trip. *Exp. Fluids* **52**, 865-876.
Erm, L. P. and Joubert, P. N. (1991). Low-Reynolds-number turbulent boundary layers. *J. Fluid Mech.* **230**, 1-44.
Fish, F. E. and Battle, J. M. (1995). Hydrodynamic design of the humpback whale flipper. *J. Morphol.* **225**, 51-60.
Fransson, J. H. M., Matsubara, M. and Alfredsson, P. H. (2005). Transition induced by free-stream turbulence. *J. Fluid Mech.* **527**, 1-25.
Gibbings, J. C. (1959). *On Boundary Layer Transition Wires (Technical Report 462)*. London: ARC.
Giguère, P. and Selig, M. S. (1999). Aerodynamic effects of leading-edge tape on aerofoils at low Reynolds numbers. *Wind Energy* **2**, 125-136.
Gopalarathnam, A., Broughton, B. A., McGranhan, B. D. and Selig, M. S. (2003). Design of low reynolds number airfoils with trips. *J. Aircraft* **40**, 768-775.
Harleman, M. (2012). On the effect of turbulence on bubbles. PhD thesis, Delft University of Technology, Delft.
Hefner, J. N. and Sabo, F. E. (1987). Research in natural laminar flow and laminar-flow control. *Proceedings of a symposium sponsored by the National Aeronautics and Space Administration*. Langley Research Center, Hampton, VA: NASA.
Henningsson, P. and Hedenström, A. (2011). Aerodynamics of gliding flight in common swifts. *J. Exp. Biol.* **214**, 382-393.
Holmes, B. J., Obara, C. J. and Yip, L. P. (1984). *Natural Laminar Flow Experiments on Modern Airplane Surfaces (Technical Paper 2256)*. Hampton, VA: NASA.
Hord, K. and Liang, Y. (2012). Numerical investigation of the aerodynamic and structural characteristics of a corrugated airfoil. *J. Aircraft* **49**, 749-757.
Jongerius, S. R. and Lentink, D. (2010). Structural analysis of a dragonfly wing. *Exp. Mech.* **50**, 1323-1334.
Kesel, A. B. (2000). Aerodynamic characteristics of dragonfly wing sections compared with technical aerofoils. *J. Exp. Biol.* **203**, 3125-3135.
Kim, W.-L., Ko, J. H., Park, H. C. and Byun, D. (2009). Effects of corrugation of the dragonfly wing on gliding performance. *J. Theor. Biol.* **260**, 523-530.
Klebanoff, P. S. (1955). *Characteristics of Turbulence in A Boundary Layer with Zero Pressure Gradient (NACA report 1247)*. Washington: NACA.
Kraemer, K. (1961). Über die wirkung von stölperdrähten auf den grenzschichtumschlag. *Z. Flugwissensch* **9**, 20-27.
Kruyt, J. W., Quicazán-Rubio, E. M., van Heijst, G. F., Altshuler, D. L. and Lentink, D. (2014). Hummingbird wing efficacy depends on aspect ratio and compares with helicopter rotors. *J. R. Soc. Interface* **11**, 12.
Kundu, P. and Cohen, L. (2007). *Fluid Mechanics*. Waltham, MA: Academic Press.
Lentink, D. and de Kat, R. (2014). Gliding swifts attain laminar flow over rough wings. *PLoS ONE* **9**, e99901.
Lentink, D. and Gerritsma, M. (2003). Influence of airfoil shape on performance in insect flight. *Proceedings of 33rd AIAA fluid dynamics conference and exhibit*. Orlando, FL: AIAA.
Lentink, D., Müller, U. K., Stamhuis, E. J., De Kat, R., Van Gestel, W., Veldhuis, L. L. M., Henningsson, P., Hedenström, A., Videler, J. and van Leeuwen, J. L. (2007). How swifts control their glide performance with morphing wings. *Nature* **446**, 1082-1085.
Levy, D.-E. and Seifert, A. (2009). Simplified dragonfly airfoil aerodynamics at Reynolds numbers below 8000. *Phys. Fluids* **21**, 071901.
Levy, D.-E. and Seifert, A. (2010). Parameter study of simplified dragonfly airfoil geometry at Reynolds number of 6000. *J. Theor. Biol.* **266**, 691-702.
Lian, Y. and Shyy, W. (2007). Laminar-turbulent transition of a low Reynolds number rigid or flexible airfoil. *AIAA J.* **45**, 1501-1513.
Lissaman, P. B. S. (1983). Low-Reynolds-number airfoils. *Annu. Rev. Fluid Mech.* **15**, 223-239.
Lyon, C. A., Selig, M. S. and Broeren, A. P. (1997). Boundary layer trips on airfoils at low Reynolds numbers. *35th Aerospace sciences meeting & exhibit*, Reno, NV: AIAA.
McGuire, J. A., Witt, C. C., Remsen, J. V., Jr, Corl, A., Rabosky, D. L., Altshuler, D. L. and Dudley, R. (2014). Molecular phylogenetics and the diversification of hummingbirds. *Curr. Biol.* **24**, 910-916.
Miklosovic, D. S., Murray, M. M., Howle, L. E. and Fish, F. E. (2004). Leading-edge tubercles delay stall on humpback whale (Megaptera novaeangliae) flippers. *Phys. Fluid.* **16**, L39-L42.

Mueller, T. J. (1999). *Aerodynamic Measurements at Low Reynolds Number for Fixed Wing Micro-Air Vehicles*. RTO AVT/VKI Special course on development and operation of UAVs for military and civil applications. Belgium: VKI.
Mueller, T. J. (2002). *Fixed and Flapping Wing Aerodynamics for Micro Air Vehicle Applications*. Reston, VA: AIAA.
Muijres, F. T., Johansson, L. C., Bowlin, M. S., Winter, Y. and Hedenström, A. (2012). Comparing aerodynamic efficiency in birds and bats suggests better flight performance in birds. *PLoS ONE* **7**, e37335.
Murphy, J. T. and Hu, H. (2010). An experimental study of a bio-inspired corrugated airfoil for micro air vehicle applications. *Exp. Fluids* **49**, 531-546.
Mydlarski, L. and Warhaft, Z. (1996). On the onset of high-Reynolds-number grid-generated wind tunnel turbulence. *J. Fluid Mech.* **320**, 331-368.
Nudds, R. L. and Dyke, G. J. (2010). Narrow primary feather rachises in Confuciusornis and Archaeopteryx suggest poor flight ability. *Science* **328**, 887-889.
Pedro, H. and Kobayashi, M. H. (2008). Numerical study of stall delay on humpback whale flippers. *46th AIAA Aerospace Sciences Meeting and Exhibit*, Reno, NV: AIAA.
Pennycuick, C. J. (2008). *Modelling the Flying Bird*. Burlington, MA: Elsevier.
Preston, J. H. (1958). The minimum Reynolds number for a turbulent boundary layer and the selection of a transition device. *J. Fluid Mech.* **3**, 373-384.
Rees, C. J. C. (1975a). Aerodynamic properties of an insect wing section and a smooth aerofoil compared. *Nature* **258**, 141-142.
Rees, C. J. C. (1975b). Form and function in corrugated insect wings. *Nature* **256**, 200-203.
Schlichting, H. (1979). *Boundary Layer Theory*. New York, USA: McGraw-Hill.
Schmidt, G. S. and Mueller, T. J. (1989). Analysis of low Reynolds number separation bubbles using semi-emperical methods. *AIAA J.* **27**, 993-1001.
Schröder, A., Geisler, R., Staack, K., Elsinga, G. E., Scarano, F., Wieneke, B., Henning, A., Poelma, C. and Westerweel, J. (2011). Eulerian and Lagrangian views of a turbulent boundary layer flow using time-resolved tomographic PIV. *Exp. Fluids* **50**, 1071-1091.
Shyy, W. (2013). *An Introduction to Flapping Wing Aerodynamics*. Cambridge: Cambridge University Press.
Simons, M. (1994). *Model Aircraft Aerodynamics*. Argus Books.
Spedding, G. R. and Hedenström, A. (2009). PIV-based investigations of animal flight. *Exp. Fluids* **46**, 749-763.
Spedding, G. R., Hedenström, A. H., McArthur, J. and Rosen, M. (2008). The implications of low-speed fixed-wing aerofoil measurements on the analysis and performance of flapping bird wings. *J. Exp. Biol.* **211**, 215-223.
Taylor, H. D. (1947). *The Elimination of Diffuser Separation by Vortex Generators (R-4012-3)*. United Aircraft Corporation Report R-4012-3.
van Nierop, E. A., Alben, S. and Brenner, M. P. (2008). How bumps on whale flippers delay stall: an aerodynamic model. *Phys. Rev. Lett.* **100**, 054502.
Vargas, A. and Mittal, R. (2004). Aerodynamic performance of biological airfoils. *2nd AIAA Flow Control conference*, Portland, OR: AIAA.
Videler, J. J. (2006). *Avian Flight*. Oxford: Oxford University Press.
Videler, J. J., Stamhuis, E. J. and Povel, G. D. E. (2004). Leading-edge vortex lifts swifts. *Science* **306**, 1960-1962.
White, F. M. (1991). *Viscous Fluid Flow*. New York, USA: McGraw-Hill.
Winzen, A., Roidl, B., Klän, S., Klaas, M. and Schröder, W. (2014). Particle-image velocimetry and force measurements of leading-edge serrations on owl-based wing models. *J. Bionic Eng.* **11**, 423-438.
Yuan, W., Mahmood, K., Windte, J., Scholz, U. and Radespiel, R. (2005). An investigation of low-Reynolds-number flows past airfoils. *23rd AIAA Apllied aerodynamics conference*, Toronto, Canada: AIAA.